# Crystallization Behavior of Syndiotactic Polystyrene Nanocomposites for Melt- and Cold-Crystallizations

**Chen-Rui Tseng,[1] Shoei-Chin Wu,[1] Jeng-Jue Wu,[2] Feng-Chih Chang[1]**

[1] *Institute of Applied Chemistry, National Chiao-Tung University, Hsin-Chu, 30043,Taiwan, R.O.C.*
[2] *Department of Chemical Engineering, National Chung-Hsing University, Tai-Chung, Taiwan, R.O.C.*

Received 26 November 2001; accepted 14 January 2002

**ABSTRACT:** Analyses of the effects of montmorillonite (clay) on the crystallinity and crystallization behavior of syndiotactic polystyrene (s-PS) were investigated by Fourier transform infrared (FTIR) spectroscopy and differential scanning calorimetry (DSC). The dispersibility of the clay in s-PS nanocomposites was studied by X-ray and transmission electron microscopy (TEM). The clay was dispersed into the s-PS matrix by melt blending on a scale of 1–2 nm or few tenths–100 nm, depending on the surfactant treatment. On adding clay, the crystallization behavior of the s-PS tends to convert into the $\beta$-crystal from the $\alpha$-crystal after being cold-crystallized because the clay plays a vital role in facilitating the formation of the thermodynamically favored $\beta$-form crystal when the s-PS is cold- or melt-crystallized. This phenomenon leads to a change in a conventional mechanism of molecular packing for the s-PS. Evidently, the clay significantly affects the crystallinity and crystallization behavior of the s-PS. © 2002 Wiley Periodicals, Inc. J Appl Polym Sci 86: 2492–2501, 2002

**Key words:** syndiotactic polystyrene (s-PS); clay; nanocomposites; surfactant; crystallization

## INTRODUCTION

The synthesis of stereoregular polystyrene has been developed to produce nearly 100% syndiotactic conformation using a specific metallocence catalyst.[1–3] Syndiotactic polystyrene (s-PS) differs from other polystyrenes (such as a-PS and i-PS) in that phenyl rings regularly alternate from side to side with respect to the polymer chain backbone. This highly stereoregular s-PS has attracted increasing attention because of its commercial importance. s-PS can be crystallized into two different chain conformations, helical and trans. Helical trans-trans and gauche-gauche (TTGG) chain conformations are formed in the solution-recovered s-PS, whereas the more favorable all-trans (TTTT) conformations are formed either from the melt or from annealing at elevated temperatures.[4–8]

Blends of thermoplastic polymers with montmorillonite have been extensively studied because a small amount of well-dispersed clay in a polymer matrix can improve their mechanical properties, optical properties, and magnetic behavior.[9–12] There are two main approaches by which polymer is intercalated into the silicate layers of clay mineral; one is the insertion of a suitable monomer and subsequent polymerization, and the other is the direct insertion of polymer chains from solution or melt state. Silicate layers well dispersed in nylon 6 matrix has been accomplished by the first method.[13, 14] This nylon hybrid exhibits superior properties, such as high strength, high modulus, and high heat distortion temperature, compared with the virgin nylon 6.[15, 16] The clay of a polymer–clay hybrid can be more thoroughly dispersed on a nanometer scale by inserting the polymer chains into the silicate interlayers of the clay if the clay is pretreated by an appropriate surfactant.[17]

In our previous studies, we have investigated the chain conformation and crystallization behaviors of s-PS–clay hybrids by using polymer intercalation from the solution into the montmorillonite.[17–19] At least two important factors need to be considered to achieve the homogeneous dispersion of the clay layers in the s-PS hybrids. First, the surfactant should be intercalated between silicate layers of clay by ionic bonding. Second, the hydrophobic tail of the surfactant molecule should be partially compatible or interacted with s-PS molecules. The crystallization rate of s-PS–clay nanocomposites is significantly faster than that of the pure s-PS.[18]

Fourier transform infrared (FTIR) spectroscopic techniques have been extensively applied to assess polymer crystallinity and chain conformation. As a highly effective means of structurally characterizing polymers, FTIR complements other techniques in providing detailed information about chain conformation changes and the crystallinity of crystalline polymers that is nondestructive and fast.[20–22]

In this study, we prepare s-PS–clay nanocomposites using polymer intercalation by melt blending. Both transmission electron microscopy (TEM) and X-ray

*Correspondence to:* F-C. Chang (changfc@cc.nctu.edu.tw).

Journal of Applied Polymer Science, Vol. 86, 2492–2501 (2002)

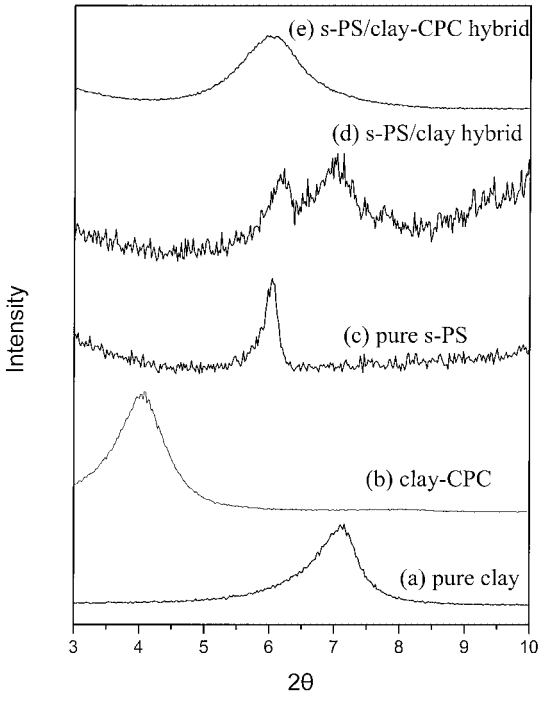


**Figure 1** X-ray diffraction patterns ranging from $2\theta = 3$–$10°$ for (a) pure clay; (b) pure $\beta$-form of s-PS; (c) s-PS–clay hybrid; and (d) s-PS–clay/CPC hybrid.

analyses are used to characterize clay dispersibility in the s-PS matrix. FTIR is applied to characterize the changes of crystalline form and crystallinity in the s-PS containing clay. Differential scanning calorimetry (DSC) analyses are also conducted to examine the effect of the clay on the crystallization behavior of s-PS–clay nanocomposites. Two goals are pursued: (1) detailed characterization of crystallization behavior and morphology of the s-PS caused by clay dispersibility; and more importantly, (2) examination of the effect of clay dispersibility on crystallinity of s-PS thin film samples during melt- and cold-crystallization. The observed crystallization behavior and crystallinity provide valuable information regarding the effect of clay on crystallization behavior of the s-PS.

## EXPERIMENTAL

### Materials

The s-PS was synthesized using a homogeneous catalyst consisting of $CpTiCl_3$ and methylalumoxane (MAO) in toluene,[5] with $M_n$ = 100,000. The chemical structure of the s-PS, with [rr] = 99%, was identified by a solution carbon-13 nuclear magnetic resonance

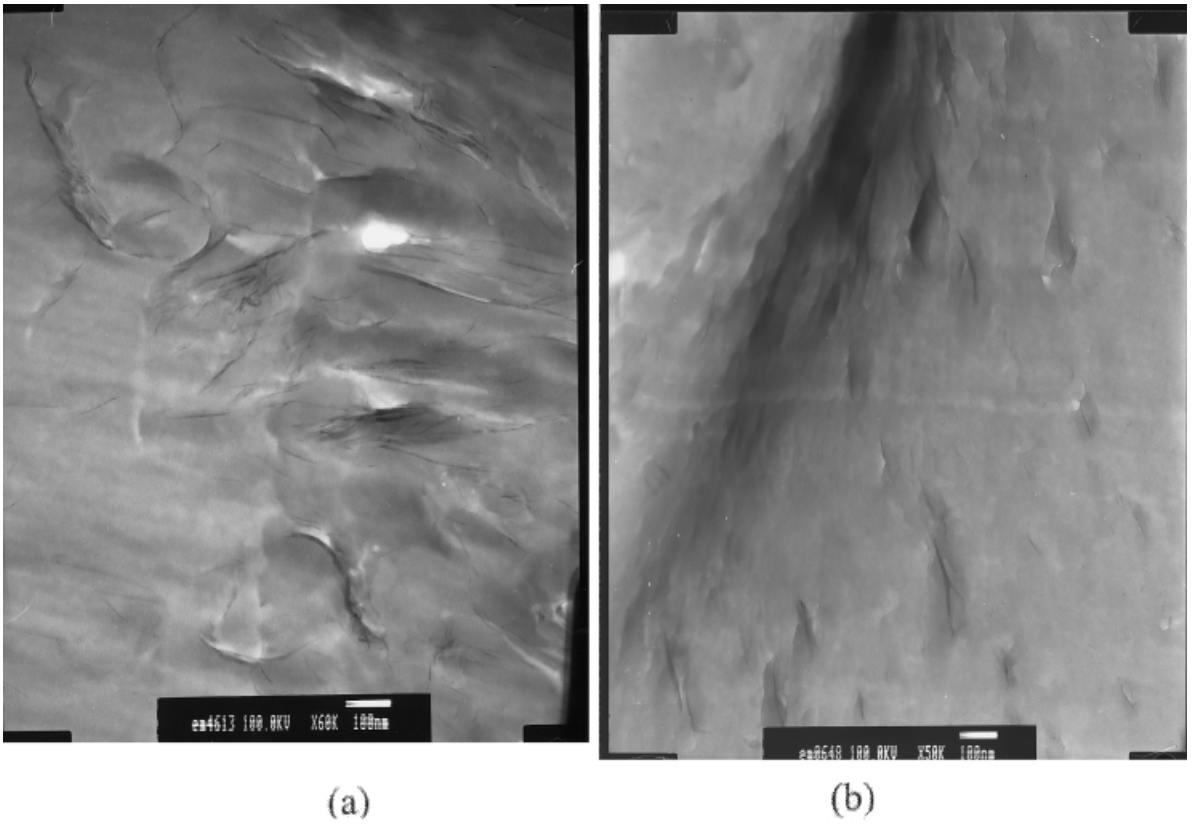


**Figure 2** TEM micrographs of thin sections of (a) s-PS–clay/CPC hybrid and (b) s-PS–clay hybrid obtained from melt blending without thermal treatment.

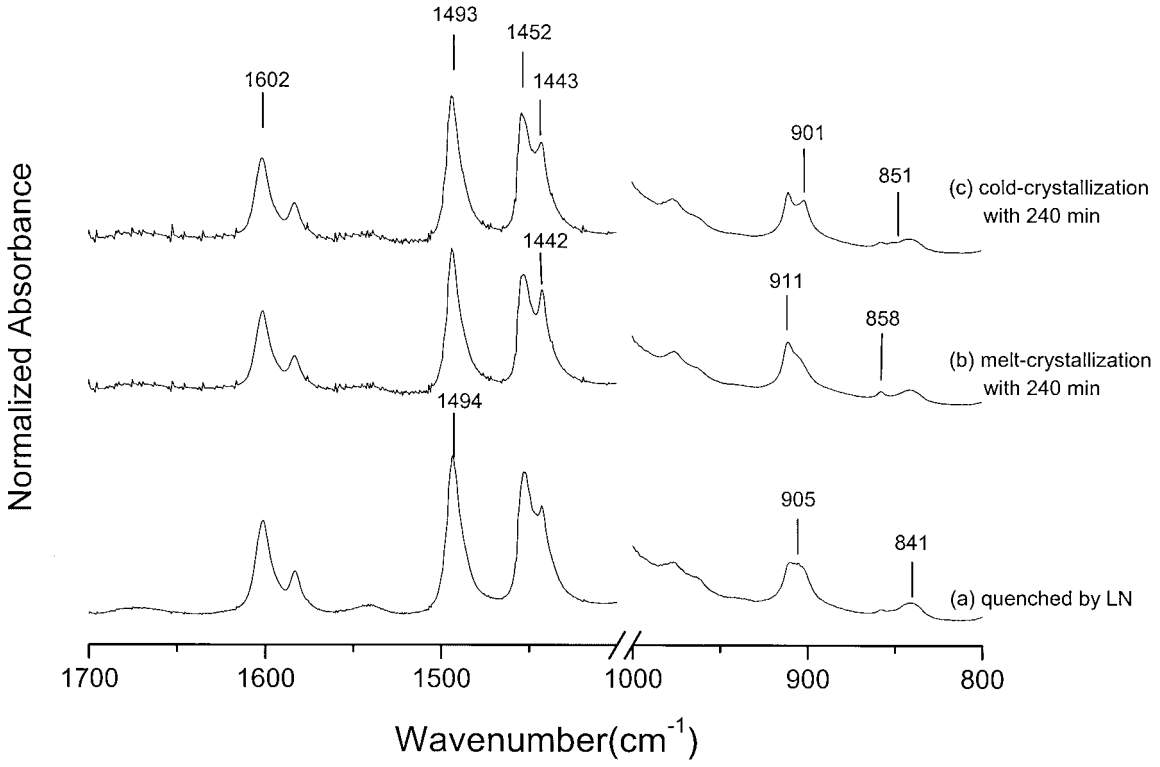


**Figure 3** FTIR spectra of the s-PS ranging from 1700 to 800 $cm^{-1}$: (a) amorphous s-PS annealed at 320°C for 10 min and quenched by LN, (b) $\beta$-form s-PS: annealed at 320°C for 10 min and melt-crystallized at 240°C/min, (c) $\alpha$- and $\beta$-forms s-PS annealed at 320°C for 10 min and cold-crystallized at 240°C/min.

spectroscopy ($^{13}C$ NMR) spectrum.[23] The Montmorillonite 'Kunipia F' (clay) was supplied by the Kunimine Company of Japan. This clay mineral bears exchangeable sodium ions with exchange capacity of ~119 meq~100 g. Cetyl pyridium chloride (CPC), a cationic surfactant, purchased from Sigma, has a purity of >99%.

### Preparation of organophilic clay mineral

Sodium montmorillonite (1 g), CPC (0.39 g), and 50 mL of distilled water were placed in a 100-mL beaker; the clay/CPC equivalent ratio = 1:1. The mixture was stirred vigorously for 8 h and then filtered, washed, freeze-dried, and kept in a vacuum oven at room temperature for 24 h. This organically modified clay (denoted as "clay/CPC" in following text) was hydrophobic.

### Preparation of s-PS–clay hybrids

Melt blending of the s-PS and clay or clay/CPC was carried out on a corotating 30-min twin-screw extruder ($L/D$ = 36, Sino-Alloy Machinery Inc.). The extruder barrel temperatures were set at 270–290°C, and a rotational speed of 250 rpm was employed.

### Characterizations

#### DSC dynamical and isothermal crystallization

DSC (DSC 2010, Du Pont) was used for determining the melting transition temperature ($T_m$) and melting enthalpy ($\Delta H_m$) of the s-PS. Five to ten milligrams of the s-PS–clay or s-PS–clay/CPC hybrid in an aluminum pan was heated in the DSC furnace to 320°C and kept at that temperature for 10 min to ensure total relaxation of the sample and to eliminate the influence of thermal history. Isothermal cold- and melt-crystallization were performed in an environmental chamber equipped with a temperature-programmable controller with an accuracy of ±0.1°C. For melt-crystallization, the sample was heated to 320°C, quickly cooled (−100°/min) to 240°C for various durations, and then reheated from 240 to 310°C at a heating rate of 10°/min. For cold-crystallization, the sample was quenched by liquid nitrogen of the melt at 320°C, then reheated to 240°C at a rate of 100°C/min, maintained at 240°C isothermally for various durations, and then reheated from 240 to 310°C at a heating rate of 10°C/min. All experiments were carried out under continuous nitrogen flow to ensure minimal sample oxidation or degradation.

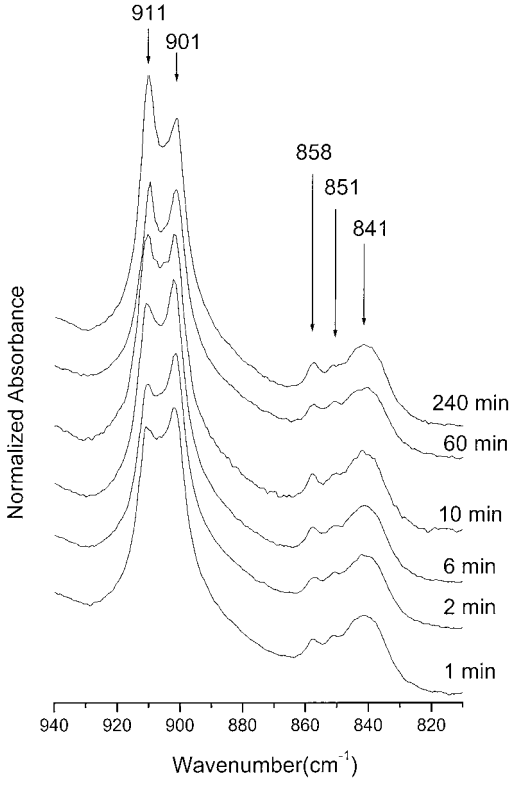


**Figure 4** FTIR spectra of s-PS–clay hybrid cold-crystallized isothermally at 240°C for various crystallization durations.

### Infrared spectra

Infrared spectra were obtained at a resolution of 1.0 $cm^{-1}$ by FTIR (Nicolet AVATAR 320 FTIR spectrometer) at 30°C, ranging from 4000 to 400 $cm^{-1}$. The frequency scale was internally calibrated using a He-Ne laser, and 32 scans were single-averaged to reduce the noise. The crystal form determination of s-PS–clay and s-PS–clay/CPC hybrids by FTIR was carried out in the melt- and cold-crystallization at 240°C for various durations and then quenched by liquid nitrogen. The thickness of the s-PS sample was controlled at $<10$ $\mu$m to minimize the effect of thickness on crystallization.

### Wide-angle X-ray diffraction

X-ray diffraction spectra were collected on a X-ray diffraction instrument (M18XHF-SRA, MacScience Company, Japan), using CoK$\alpha$ radiation, and Bragg's Law ($\lambda = 2d \sin \theta$) was used to compute the spacing.

### Transmission electron microscopy (TEM)

A TEM micrograph of a microtomed section of the s-PS–clay hybrid of 60–100 nm thickness, mounted in epoxy, was prepared with a transmission electron microscope (JEM-2000FX, Joel Company, Japan) at an acceleration voltage of 100 kV.

## RESULTS AND DISCUSSION

### Clay dispersibility

The clay dispersibility in the s-PS matrix can be obtained from the X-ray diffraction pattern. The X-ray diffraction patterns in the range $2\theta$ = 3–10° for clay, clay/CPC, pure s-PS, s-PS–clay (95:5), and s-PS–clay/CPC (95:5), in which the clay/CPC ratio = 1:1, are shown in Figures 1a–1e, respectively. The X-ray diffraction pattern of the pure clay that contains basal reflections of the non-intercalated repeat distance, $d$, of 1.2 nm ($2\theta$ = 7.1°) is shown in Figure 1a.The one sharp peak ($2\theta$ = 6.1°) in Figure 1c corresponds to the pure $\beta$-form s-PS crystal.[7, 8, 24, 25] Two peaks at $2\theta$ = 6.9° and 6.1°, shown in Figure 1d, correspond to the pure clay and the $\beta$-form s-PS crystal, respectively. Only one wide peak at $2\theta$ = 6.1° is found in Figure 1e, which belongs to the $\beta$-form crystal of the s-PS,[17, 18] whereas the characteristic peak from the clay disappears totally. Comparing the results shown in Figures 1d and 1e reveals that the clay appears delaminated and dispersed completely within the s-PS matrix when the clay is pretreated by the CPC surfactant. The s-PS chains can be more easily intercalated into the narrow space of the oriented collections of parallel silicate layers by the CPC pretreatment.

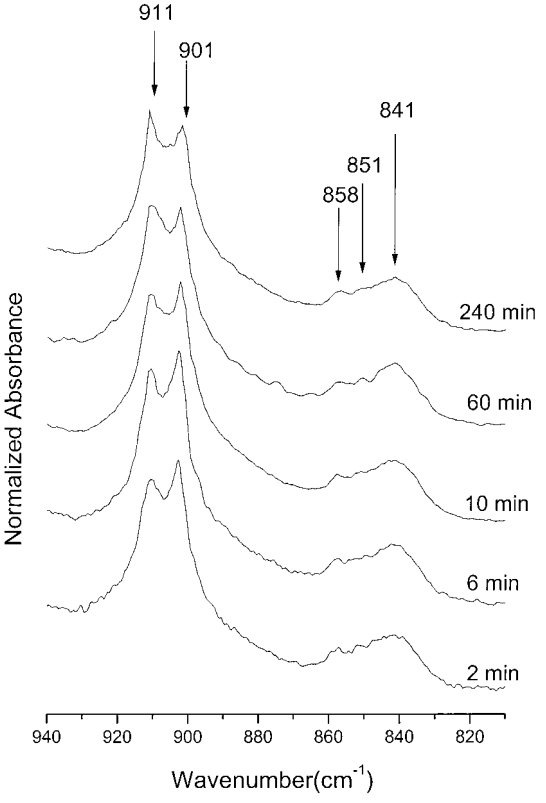


**Figure 5** FTIR spectra of s-PS–clay/CPC hybrid cold-crystallized isothermally at 240°C for various crystallization durations.

**TABLE I**
**Data of IR Curve Fitting 865–825 $cm^{-1}$ of Cold-Crystallized s-PS/Clay Hybrid**

| Cold-Crystallization Isothermal Duration (min) | Amorphous Freq.[a] ($cm^{-1}$) | $\alpha$ Form Freq.[a] ($cm^{-1}$) | $\beta$ Form Freq.[a] ($cm^{-1}$) | Area[b] of Amorphous | Area[b] of $\alpha$ Form | Area[b] of $\beta$ Form | Absolute Crystallinity, $C_\alpha$ (%) | Absolute Crystallinity, $C_\beta$ (%) |
|---|---|---|---|---|---|---|---|---|
| 240 | 840.9 | 851.4 | 857.6 | 0.768 | 0.087 | 0.145 | 27.3 | 29.8 |
| 60 | 840.7 | 851.6 | 857.8 | 0.770 | 0.110 | 0.120 | 33.7 | 24.2 |
| 10 | 841.0 | 851.5 | 857.7 | 0.771 | 0.110 | 0.119 | 33.8 | 24.0 |
| 6 | 840.7 | 851.8 | 857.9 | 0.774 | 0.130 | 0.096 | 39.3 | 19.0 |
| 2 | 840.4 | 851.7 | 857.8 | 0.775 | 0.151 | 0.074 | 44.7 | 14.4 |
| 1 | 840.9 | 851.6 | 857.6 | 0.810 | 0.113 | 0.077 | 36.7 | 16.4 |

[a] Wavenumber.
[b] Absorbance area ranging from 865 to 825 $cm^{-1}$ assumed to be 1.

The TEM micrographs of thin sections of s-PS–clay/CPC (95:5) and s-PS–clay (95:5) hybrids after melt blending are shown in Figures 2a and 2b, respectively. Figure 2a contains the TEM bright field image of the s-PS–clay/CPC hybrid, where the dark lines denote the silicate layers. The surfactant, CPC, accommodates the intercalated clay by the organic cation and renders the hydrophobic silicate surface organophilic. For s-PS–clay/CPC, the stacked silicate layers of ~1–5 nm thickness (~1–3 parallel silicate layers) are randomly distributed in the s-PS matrix. The results in Figure 2b show that the untreated clay in the s-PS matrix is not well dispersed, indicating that the layers of clay are unexfoliated. The clay layers shown in Figure 2b are relatively rougher and more agglomerated than those of Figure 2a. These observations correlate well with the X-ray diffraction (XRD) patterns.

## Infrared characterization

s-PS has received considerable interest because of its pluralistic crystallizations in recent years.[1, 4, 7, 8, 26] Four distinct polymorphs ($\alpha$-, $\beta$-, $\gamma$-, and $\delta$-forms) have been identified[26] that can be divided into two groups: (i) $\gamma$- and $\delta$-forms possessing a helical TTGG chain conformation and (ii) $\alpha$- and $\beta$-forms possessing a planar TTTT "zigzag" conformation. Notably, the desired crystal must be prepared to correlate the characteristic absorbance in FTIR spectrum with a specific chain conformation and crystal forms. The FTIR spectra ranging from 1700 to 1400 and 1000 to 800 $cm^{-1}$ of s-PS–clay (95:5) hybrids in amorphous, $\alpha$-, and $\beta$-forms, as prepared according to procedures described elsewhere,[26] are shown in Figure 3. The following description on FTIR vibrational spectroscopic features with respect to the variation of the s-PS crystalline structure is based on reported literature[4–6, 18–20] and our observations. The characteristic peaks of amorphous s-PS are 1494, 905, and 841 $cm^{-1}$, as shown in Figure 3a. The specific peaks of the $\beta$-form at 1442, 911 (shifted from 905 $cm^{-1}$), and 858 (shifted from 841 $cm^{-1}$) $cm^{-1}$ are shown in Figure 3b. The specific peaks of the $\alpha$-form at 1443, 901 (shifted from 905 $cm^{-1}$), and 851 (shifted from 841 $cm^{-1}$) $cm^{-1}$ are shown in Figure 3c. These spectral baselines have been offset to clearly indicate changes through different thermal histories. The peak position and intensity of the 1602 $cm^{-1}$ peak (corresponding to benzene ring, as shown in Figure 3) remain unaffected by varying either the chain conformation or crystallinity in these s-PS FTIR spectra. Therefore, all peak areas in the range have been normalized by the 1602 $cm^{-1}$ peak area. This procedure provides an efficient and reliable means of identifying and quantifying different crystal forms present in the s-PS nanocomposite. To more clearly understand the change caused by adding the clay, we are particularly interested in the IR spectra ranging from 940 to 820 $cm^{-1}$, which is highly sensitive to chain packing for the s-PS polymorph.[18–20, 27, 28] It is well known that the thermodynamically favored

**TABLE II**
**Data of IR curve fitting 865–825 $cm^{-1}$ of Cold-Crystallized s-PS/Clay–CPC Hybrid**

| Cold-Crystallization Isothermal Duration (min) | Amorphous Freq.[a] ($cm^{-1}$) | $\alpha$ Form Freq.[a] ($cm^{-1}$) | $\beta$ Form Freq.[a] ($cm^{-1}$) | Area[b] of Amorphous Form | Area[b] of $\alpha$ Form | Area[b] of $\beta$ Form | Absolute Crystallinity, $C_\alpha$ (%) | Absolute Crystallinity, $C_\beta$ (%) |
|---|---|---|---|---|---|---|---|---|
| 240 | 840.8 | 851.4 | 857.7 | 0.750 | 0.095 | 0.155 | 28.8 | 30.7 |
| 60 | 841.4 | 851.1 | 856.5 | 0.755 | 0.108 | 0.137 | 32.5 | 27.0 |
| 10 | 841.9 | 852.0 | 858.0 | 0.769 | 0.150 | 0.081 | 44.1 | 15.6 |
| 6 | 840.7 | 852.2 | 858.2 | 0.768 | 0.184 | 0.048 | 52.3 | 8.9 |
| 2 | 840.2 | 851.2 | 858.3 | 0.787 | 0.176 | 0.037 | 51.7 | 7.1 |

[a] Wavenumber.
[b] Absorbance area ranging from 865 to 825 $cm^{-1}$ assumed to be 1.

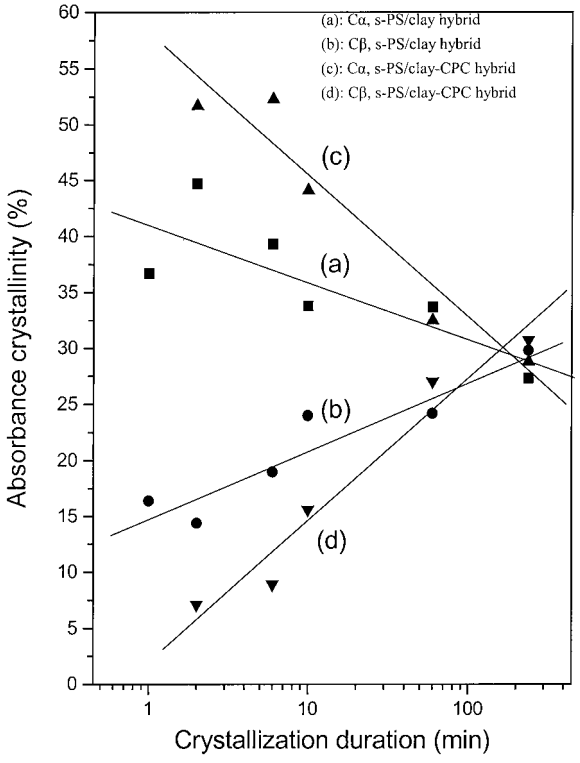


**Figure 6** The relationship between crystallinity of cold-crystallized s-PS hybrids and crystallization duration: (a) $C_\alpha$, s-PS–clay hybrid; (b) $C_\beta$, s-PS–clay hybrid; (c) $C_\alpha$, s-PS–clay/CPC hybrid; and (d) $C_\beta$, s-PS–clay/CPC hybrid.

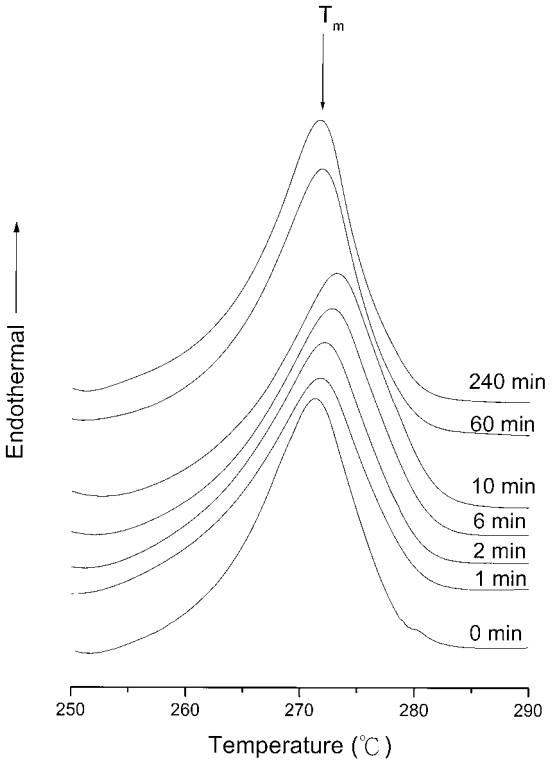


**Figure 7** DSC thermogram with heating scan of 10°C/min of s-PS–clay hybrid vold-crystallizedisothermally at 240°C for various crystallization durations.

$\beta$-form of s-PS is formed by melt-crystallization at a high temperature.[18, 22] The newborn bands appearing at 911 and 858 $cm^{-1}$correspond to the $\beta$-crystal when the s-PS–clay is melt-crystallized at 240°C for 240 min and then quenched by liquid nitrogen. The characteristic peaks of the $\alpha$-crystal are absent, as shown in Figure 3b. The results in Figure 3c reveal the existence of both $\alpha$- and $\beta$-crystal phase peaks when the s-PS–clay hybrid is cold-crystallized at 240°C for 240 min and then quenched by liquid nitrogen.

The absolute crystallinities of $\alpha$- and $\beta$-forms of the s-PS can be calculated from the following equations:[18]

$$C_\alpha = \frac{A_{851}/a_\alpha}{A_{841} + A_{851}/a_\alpha + A_{858}/a_\beta} \quad (1)$$

$$C_\beta = \frac{A_{858}/a_\beta}{A_{841} + A_{851}/a_\alpha + A_{858}/a_\beta} \quad (2)$$

where $C_\alpha$ and $C_\beta$ represent the crystallinities of $\alpha$- and $\beta$ forms, respectively; and $A_{841}$, $A_{851}$, and $A_{858}$ are area fractions of amorphous, $\alpha$-, and $\beta$- forms, respectively, as obtained by the absorbance areas ranging from 865 to 825 $cm^{-1}$. The conversion coefficients $a_\alpha$ and $a_\beta$ of 0.178 and 0.272, respectively, based on our previous reports,[18, 19] are the respective ratios of absorptive co-

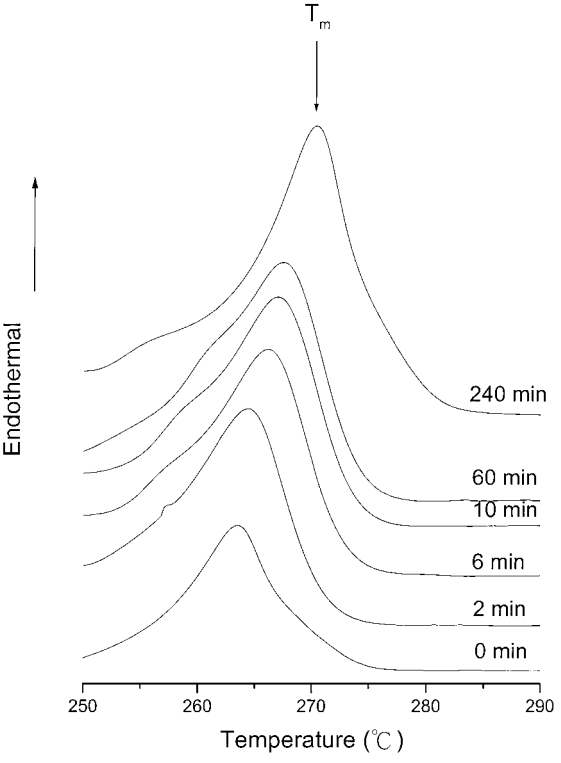


**Figure 8** DSC thermogram with heating scan of 10°C/min of s-PS–clay/CPC hybrid cold-crystallizedisothermally at 240°C for various crystallization durations.

**TABLE III**
**Thermal Properties of Cold-Crystallized s-PS/Clay and s-PS/Clay–CPC Hybrids**

| Cold-crystallization Isothermal duration (min) | s-PS/Clay Hybrid | | s-PS/Clay–CPC Hybrid | |
|---|---|---|---|---|
| | $T^{\alpha+\beta_m}$ (°C) | $\Delta H^{\alpha+\beta}$ (J/M) | $T^{\alpha+\beta_m}$ (°C) | $\Delta H^{\alpha+\beta}$ (J/M) |
| 240 | 271.5 | 25.7 | 270.4 | 22.4 |
| 60 | 271.8 | 24.3 | 267.6 | 19.7 |
| 10 | 273.0 | 23.7 | 267.2 | 17.3 |
| 6 | 272.6 | 23.7 | 266.3 | 15.4 |
| 2 | 272.0 | 23.7 | 264.6 | 14.3 |
| 0 | 271.0 | 21.6 | 263.8 | 10.5 |

efficients $A_{851}/A_{841}$ and $A_{858}/A_{841}$ for $\alpha$- and $\beta$-form crystal absorbances, respectively.

### Effects of clay on crystal form and crystallinity for cold-crystallization

The FTIR spectra of cold-crystallized s-PS–clay and s-PS–clay/CPC hybrids, crystallized at 240°C for various durations, range from 865 to 825 $cm^{-1}$ and are highly sensitive to chain packing (see Figures 4 and 5, respectively). Three peaks are particularly important in this region; they are 841, 851, and 858 $cm^{-1}$, corresponding to the amorphous phase, the $\alpha$-form crystal, and the $\beta$-form crystal, respectively. The results of curve-fitting from 865 to 825 $cm^{-1}$, absolute crystallinity, and calculated intrinsic enthalpy of cold-crystallized s-PS–clay and s-PS–clay/CPC hybrids with various isothermal durations at 240°C, obtained from Figures 4 and 5, are summarized in Tables I and II. The intensity of amorphous phase peak (841 $cm^{-1}$) decreases with increasing cold-crystallized duration as would be expected. The relationship of crystallinity versus crystallization duration for $\alpha$- and $\beta$-form crystals crystallized isothermally at 240°C, is shown in Figure 6. The crystallinity of the $\alpha$-crystal is significantly higher than that of the $\beta$-crystal, but the difference is gradually reduced with the increase of crystallization duration because the crystallization of the $\alpha$-crystal approaches its stable state faster than that of the $\beta$-crystal for the cold-crystallization processing. However, the intensities of $\alpha$-crystal peaks (901 and 851 $cm^{-1}$) decrease with increasing of the isothermal duration, whereas the intensities of $\beta$-crystal peaks (911 and 858 $cm^{-1}$) increase. This result indicates that the crystal transformation from $\alpha$- to $\beta$-crystal occurs by adding the clay or clay/CPC into the s-PS matrix during the cold-crystallization processing. The change of the crystal transformation from $\alpha$- to $\beta$-crystal in the s-PS–clay/CPC hybrid with better clay dispersion is greater than that in the s-PS–clay hybrid. The addition of clay into s-PS matrix lowers the potential energy of the $\beta$-crystal phase in the initial stage of molecular reorder to form the thermodynamically more favorable $\beta$-form of the s-PS.

The corresponding DSC thermograms of these cold-crystallized s-PS–clay and s-PS–clay/CPC hybrids obtained with a heating rate of 10°C/min from 240 to 310°C are shown in Figures 7 and 8, respectively, and the results are summarized in Table III. In the cold-crystallization, the melting point ($T_m$) and its enthalpy ($\Delta H_m$) of melting come from $\alpha$- and $\beta$-crystal phases of the s-PS. The $T_m$ of the s-PS–clay hybrid increases with increasing cold-crystallization duration until up to 10 min. This result implies that the $T_m$ (including $\alpha$- and $\beta$-crystals) of s-PS depends on the competition between kinetic and thermodynamic factors of the s-PS. The increase of $\Delta H_m$ for the s-PS–clay hybrid associates with the increase of the cold-crystallization duration. In the s-PS–clay/CPC series, both $T_m$ and $\Delta H_m$ increase significantly with the increase of the cold-crystallization duration.

### Effects of clay on crystal form and crystallinity for melt-crystallization

The FTIR spectra of isothermally cold- and melt-crystallized s-PS–clay and s-PS–clay/CPC hybrids at 240°C for 10 min are shown in Figure 9. The FTIR spectra from the cold- and the melt-crystallization processes are different. By comparing the spectra of these hybrids after cold-crystallization and melt-crystallization at 240°C, a direct measurement of the absorptivity ratio can be made. For the melt-crystallization, results of curve fitting ranging from 865 to 825 $cm^{-1}$ show two peaks that provides an adequate fitting, as shown the dash-lines in Figures 9c and 9d. These newborn bands appearing at 841 and 858 $cm^{-1}$ correspond to the amorphous phase and $\beta$-crystal when s-PS–clay and s-PS–clay/CPC hybrids are melt-crystallized.[17–19] The results of curve-fitting ranging from 865 to 825 $cm^{-1}$, absolute crystallinity, and calculated intrinsic enthalpy of melt-crystallized s-PS–clay and s-PS–clay/CPC hybrids with various isothermal durations at 240°C are summarized in Table IV. The results in Table IV reveal the intensities of the $\beta$-crystal phase peaks (858 $cm^{-1}$) from s-PS–clay and s-PS–clay/CPC hybrids prepared by melt blending increase with increasing isothermal duration at 240°C.

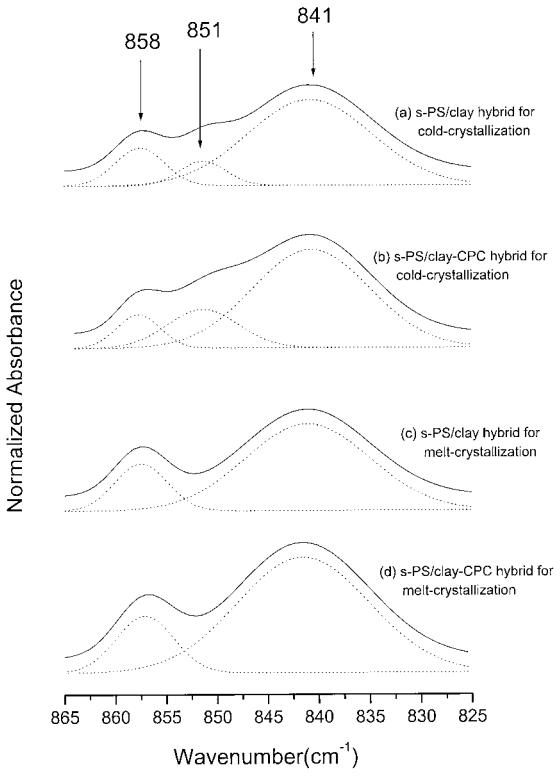


**Figure 9** FTIR spectra ranging from 865 to 825 $cm^{-1}$ of various s-PS hybrids: (a) cold-crystallized s-PS–clay hybrid; (b) cold-crystallized s-PS–clay/CPC hybrid; (c) melt-crystallized s-PS–clay hybrid; and (d) melt-crystallized s-PS–clay/CPC hybrid.

The relationship of crystallinity versus crystallization duration for the $\beta$-crystal crystallized isothermally at 240°C from melt-crystallization of s-PS–clay and s-PS–clay/CPC hybrids, based on results from Table IV, are shown in Figure 10. The results in Figure 10 also reveal that the crystallinity of the $\beta$-form crystal for the s-PS–clay hybrid is higher than that for the s-PS–clay/CPC hybrid. However, the change of the $\beta$-crystal crystallinity in Figure 10 is not as severe as that in Figure 6 when the s-PS–clay and s-PS–clay/CPC hybrids crystallized by different processes.

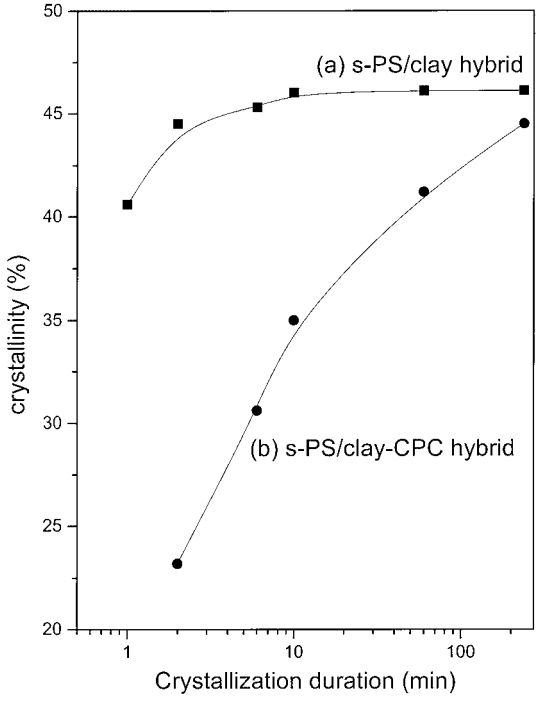


**Figure 10** The relationship between crystallinity of melt-crystallized s-PS hybrids and crystallization duration: (a) s-PS–clay hybrid and (b) s-PS–clay/CPC hybrid.

The DSC thermograms of s-PS–clay and s-PS–clay/CPC hybrids, obtained with a heating rate of 10°C/min from 240 to 310°C after melt-crystallization at 240°C for various isothermal durations, are shown in Figures 11 and 12, respectively. The thermodynamic parameter of these melt-crystallized s-PS–clay and s-PS–clay/CPC hybrids, obtained from Figures 11 and 12, are summarized in Table V. This special heating scan program attempts to avoid re-crystallization at a lower scanning temperature and the actual $T_m$ and $\Delta H_m$ of the s-PS nanocomposites can be obtained from the DSC scans. The melt-crystallized s-PS–clay hybrid at 240°C contains one major melting peak at ~269°C and one minor melting peak at ~255°C (Figure 11). The major and minor melting peaks correspond to the

**TABLE IV**
**Data of IR Curve Fitting 865–825 $cm^{-1}$ of Melt-Crystallized s-PS/Clay and s-PS/Clay–CPC Hybrids**

| | s-PS/Clay Hybrid | | | | | s-PS/clay-CPC hybrid | | | | |
|---|---|---|---|---|---|---|---|---|---|---|
| Melt-Crystallization Isothermal Duration (min) | Amorphous Freq.[a] ($cm^{-1}$) | $\beta$ Form Freq.[a] ($cm^{-1}$) | Area[b] of Amorphous Form | Area[b] of $\beta$ Form | Absolute Crystallinity, $C_\beta$ (%) | Amorphous Freq.[a] ($cm^{-1}$) | $\beta$ Form Freq.[a] ($cm^{-1}$) | Area[b] of Amorphous Form | Area[b] of $\beta$ Form | Absolute Crystallinity, $C_\beta$ (%) |
| 240 | 841.1 | 857.5 | 0.811 | 0.189 | 46.1 | 841.6 | 857.1 | 0.821 | 0.179 | 44.5 |
| 60 | 841.4 | 857.3 | 0.811 | 0.189 | 46.1 | 841.7 | 857.6 | 0.840 | 0.160 | 41.2 |
| 10 | 841.1 | 857.4 | 0.803 | 0.187 | 46.0 | 841.4 | 857.4 | 0.872 | 0.128 | 35.0 |
| 6 | 841.1 | 857.4 | 0.816 | 0.184 | 45.3 | 842.1 | 858.0 | 0.892 | 0.108 | 30.6 |
| 2 | 841.1 | 857.4 | 0.821 | 0.179 | 44.5 | 841.6 | 857.3 | 0.924 | 0.076 | 23.2 |
| 1 | 840.9 | 857.5 | 0.843 | 0.157 | 40.6 | — | — | — | — | — |

[a] Wavenumber.
[b] Absorbance area ranging from 865 to 825 $cm^{-1}$ assumed to be 1.

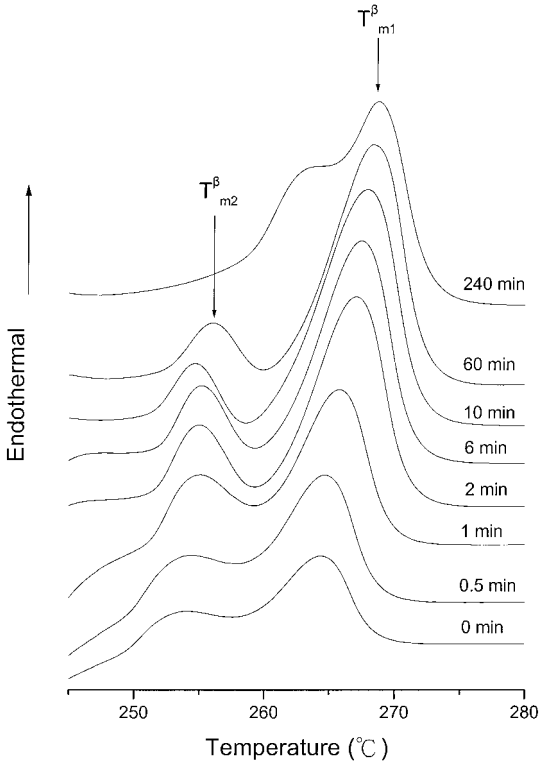


**Figure 11** DSC thermogram with heating scan of 10°C/min of s-PS–clay hybrid melt-crystallized isothermally at 240°C for various crystallization durations.

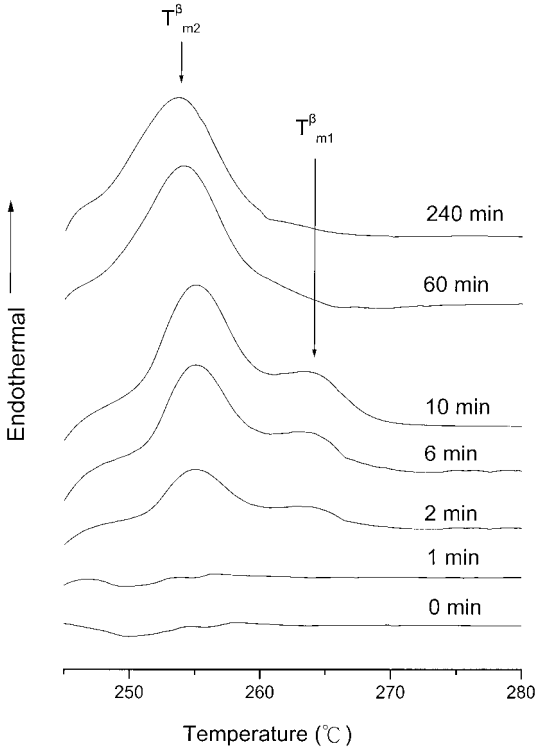


**Figure 12** DSC thermogram with heating scan of 10°C/min of s-PS–clay/CPC hybrid melt-crystallized isothermally at 240°C for various crystallization durations.

melting of the originally packed thick and thin $\beta$-crystal lamella, respectively.[17–19] Comparing the $T^{\beta}_{m1}$ and $T^{\beta}_{m2}$, reveals that the perfection of crystalline structure of the s-PS–clay hybrid in the thick lamellae is higher than that in the thin lamellae. However, for the s-PS–clay/CPC hybrid, the thick $\beta$-crystal phase peak shifts to ~265°C ($T^{\beta}_{m1}$), and the $\Delta H_m$ in the thin lamellae is higher than that in the thick lamellae, as shown in Figure 12. It is proposed that the highly dispersive clay intercalated by s-PS chains tends to increase the number of "initial nuclei" and forms the different size of $\beta$-crystal lamellae in melt-crystallization at 240°C. It has been clearly demonstrated that the presence of clay/CPC significantly affects the crystal size associated with the morphology of the s-PS. This observation suggests that the clay/CPC changes the conventional mechanism of molecular packing of the neat s-PS. The results in Figures 11 and 12 reveal that the crystallization rate is faster when the non-intercalated clay is added, because the $\beta$-crystal of melt-crystallized s-PS–clay/CPC hybrid at 240°C for 1 min is absent. The CPC molecules may interfere with the nucleation mechanism by physical hindrance within the s-PS matrix. These observations also correlate well with the FTIR spectra.

**TABLE V**
**Thermal Properties of Melt-Crystallized s-PS/Clay and s-PS/Clay–CPC Hybrids**

| Melt-Crystallization Isothermal Duration (min) | s-PS/Clay Hybrid | | | | | s-PS/Clay–CPC Hybrid | | | | |
|---|---|---|---|---|---|---|---|---|---|---|
| | $T^{\beta}_{m1}$ (°C) | $T^{\beta}_{m2}$ (°C) | $\Delta H^{\beta}_{m1}$ (J/M) | $\Delta H^{\beta}_{m2}$ (J/M) | $\Delta H^{\beta}$ (J/M) | $T^{\beta}_{m1}$ (°C) | $T^{\beta}_{m2}$ (°C) | $\Delta H^{\beta}_{m1}$ (J/M) | $\Delta H^{\beta}_{m2}$ (J/M) | $\Delta H^{\beta}$ (J/M) |
| | 264.2 | | 17.0 | | 25.8 | — | 253.6 | — | 12.5 | 12.5 |
| 240 | 269.2 | — | 8.8 | — | | | | | | |
| 60 | 268.3 | 256.1 | 21.3 | 4.1 | 25.4 | — | 254.0 | — | 12.1 | 12.1 |
| 10 | 267.9 | 254.7 | 20.5 | 3.0 | 23.5 | 263.4 | 255.1 | 3.4 | 9.4 | 11.8 |
| 6 | 267.5 | 255.2 | 20.0 | 3.3 | 23.3 | 262.9 | 255.1 | 2.5 | 6.4 | 8.9 |
| 2 | 267.1 | 255.0 | 19.4 | 3.8 | 23.2 | 263.5 | 255.0 | 1.3 | 4.6 | 5.9 |
| 1 | 266.0 | 255.7 | 15.1 | 8.4 | 23.5 | — | — | — | — | — |
| 0.5 | 264.8 | 253.0 | 14.3 | 8.2 | 22.5 | — | — | — | — | — |
| 0 | 264.3 | 252.6 | 12.1 | 8.2 | 20.3 | — | — | — | — | — |

## CONCLUSIONS

This study has provided the evidence of details for describing the mechanism of chain packing of $\alpha$- and $\beta$-crystal and crystal transformation within s-PS nanocomposites, which is affected by the addition and dispersibility of the clay in s-PS–clay and s-PS–clay/CPC hybrids. The method to determine the absolute crystallinity and crystallization behavior of $\alpha$- and $\beta$-crystal are accomplished.

As a matter of fact, the cold-crystallized s-PS shows the crystal transformation from $\alpha$- to $\beta$-crystal by adding the clay and clay/CPC into the s-PS matrix. The clay addition in the s-PS matrix lowers the $\beta$-crystal potential energy of s-PS chains in the cold-crystallization and does provide a new pathway to generate the $\beta$-form crystal in the s-PS matrix. The crystallinity of the $\beta$-form crystal appears to increase when increasing the crystallization duration and is higher from the s-PS–clay hybrid than from the s-PS–clay/CPC hybrid during the melt-crystallization. Results in this study demonstrate that the better dispersibility of the clay in the s-PS matrix changes the crystal size of $\beta$-crystal lamellae for the s-PS in the melt-crystallization.

### References


1. Ishihara, N.; Semiya, T.; Kuramoto, M.; Uoi, M. Macromolecules 1986, 19, 2464.
2. Ishihara, N.; Kuramoto, M.; Uoi, M. Macromolecules 1986, 21, 3356.
3. Zambelli, A.; Longo, P.; Pellecchia, C.; Grassi, A. Macromolecules 1987, 20, 2035.
3. Kellar, E.J.C.; Galiotis, C.; Andrews, E.H. Macromolecules 1996, 29, 3515.
4. Pellecchia, C.; Longo, P.; Grassi, A.; Ammendola, P.; Zambelli, A. Markromol Chem Rapid Commun 1987, 8, 277.
5. Musto, P.; Tavone, S.; Guerra, G.; De, R. C. J Polym Sci, Part B: Polym Phys 1997, 35, 1055.
6. Woo, E. M.; Wu, F. S. Macromol Chem Phys 1998, 199, 2041.
7. Woo, E. M.; Wu, F. S. J Polym Sci, Part B: Polym Phys 1998, 36, 2725.
8. Waddell, W. H.; O'Haver, J. H.; Evans, L. R.; Harwell, J. H. J Appl Polym Sci 1995, 55, 1627.
9. Godovski, D. Y.; Sukharev, V. Y.; Volkov, A. V. Phys Chem Solids 1993, 54, 1613.
10. Wang, Y.; Herron, N. J Phys Chem 1991, 95, 525.
11. Yang, W. Opt Comm 1987, 61, 233.
12. Vaia, R. A.; Ishii, H.; Giannelis, E. P. Chem Mater 1993, 5, 1694.
13. Usuki, A.; Kojima, Y.; Kawasumi, M.; Okada, A.; Fukushima, Y.; Kurauchi, T.; Kamigaito, O. J Mater Res 1993, 8, 1179.
14. Kojima, Y.; Usuki, A.; Kawasumi, M.; Okada, A.; Fukushima, Y.; Kurauchi, T.; Kamigaito, O. J Mater Res 1993, 8, 1185.
15. Kojima, Y.; Usuki, A.; Kawasumi, M.; Okada, A.; Kurauchi, T.; Kamigaito, O. J Appl Polym Sci 1993, 49, 1259.
16. Tseng, C. R.; Wu, J. Y.; Lee, H. Y.; Chang, F. C. 2001, Polymer 2001, 42, 10063.
17. Wu, H. D.; Tseng, C. R.; Chang, F. C. Macromolecules 2001, 34, 2992.
18. Wu, H. D.; Wu, S. C.; Wu, I. D.; Chang, F. C. Polymer 2001, 42: 4719.
19. Kellar, E. J. C.; Evan, A. M.; Knowles, J.; Galiotis, C.; Andrews, E. H., Macromolecules 1997, 30, 2400.
20. Vittoria, V.; Polym Comm 1990, 31, 263.
21. Vittoria, V.; Ruvolo Filho, A.; De Candia, F. J Macromol Sci Phys 1990, B29, 411.
22. Wang, Y.; Herron, N. J Phys Chem 1991, 95, 525.
23. De, R. C.; Rapaccuolo, M.; Guerra, G.; Petraccone, V.; Corradini, P. Polymer 1992, 33, 1423.
24. De, R. C.; Corradini, P. Macromolecules 1993, 26, 5711.
25. Guerra, G.; Vitagliano, V. M.; De Rosa, C.; Petraccone, V.; Corradini, P.; Macromolecules 1990, 23, 1539.
26. Pellecchia, C.; Longo, P.; Grassi, A.; Ammendola, P., Zambelli, A.; Markromol Chem, Rapid Commun 1987, 8, 277.
27. Musto, P.; Tavone, S.; Guerra, G., De Rosa, C. J Polym Sci B: Polym Phys 1997, 35, 1055.